



Advanced Laboratory Course

Particle Physics

Characterization of silicon strip sensors

Koen Denekamp & Riana Shaba

Advisor: Michael Windau

May 2025

ABSTRACT

The ATLAS experiment at CERN'S most powerful particle accelerator, the Large Hadron Collider (LHC), is one of the four biggest detectors in the accelerator complex where proton-proton collision events are observed and studied by particle physicists.

This laboratory report focuses on a complete study in order to understand the properties and functionalities of a silicon semiconductor detector, working with the sensor apparatus, readout electronics, and the software for data acquisition.

The Educational Alibava System (EASy), from Alibava Systems, is the software used for carrying out all the measurements. The data obtained and their processing give important insight into particle track detection.

The experimental study covers various tasks, starting with the measurement of the current-voltage characteristic to determine the depletion voltage of the silicon strip sensor. Then a signal-noise investigation was done by analyzing different scatter plots of the pedestals and noise for each strip sensor. This is followed by calibration measurements that were performed to help us with the next tasks, such as studying the structure of the strip sensors and determining the pitch, as well as exploring the charge collection efficiency of the detector by using the laser and then a radioactive β^- source, for which the data was provided to us, as we couldn't perform the measurement ourselves due to hardware malfunctions. In the end, we look at several distributions that show different behaviors of the clusters, channels forming a cluster, the strips that were hit by the detector and lastly the energy spectrum of the radioactive source.

Contents

Abstract	i
1 Introduction	2
1.1 The Large Hadron Collider	2
1.2 The ATLAS experiment	3
1.2.1 The Inner Detector (ID)	4
2 Silicon Strip Sensors	5
2.1 Semiconductors	5
2.2 The p-n junction	6
3 Experimental Setup	8
3.1 Detector Unit	9
3.2 Control Unit	10
3.3 The Alibava-gui Software	11
4 Data Analysis	12
4.1 Influence of ^{90}Y and measurement of a current-voltage characteristic	12
4.2 Pedestals and noise	13
4.3 Calibration measurements	16
4.4 Measuring the strip sensors by using the laser	17
4.5 Determination of the Charge Collection Efficiency: Using a laser	19
4.6 Determination of the Charge Collection Efficiency: Using a β^- source	22
4.7 Large source scan	23
5 Conclusions	27

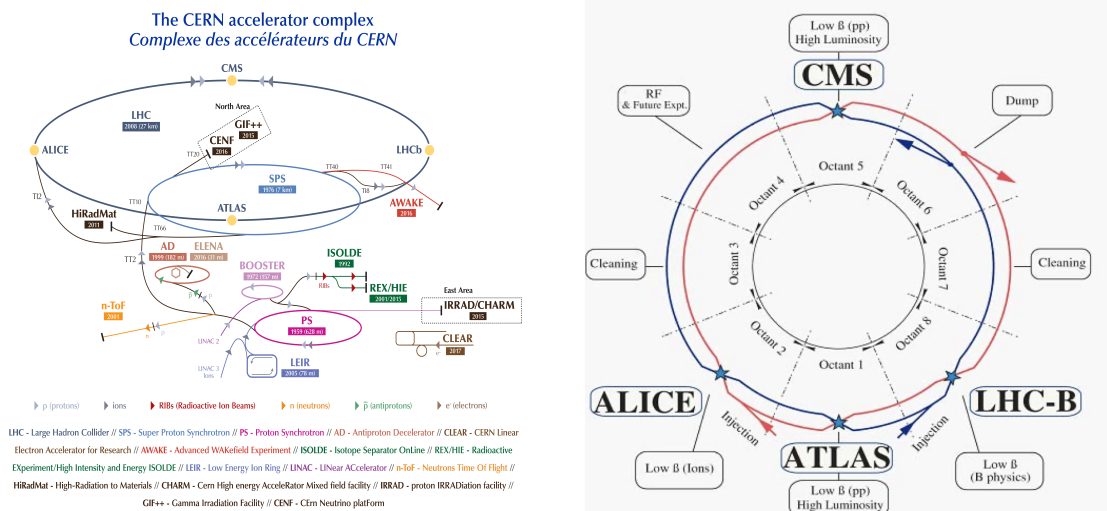
1 Introduction

1.1 The Large Hadron Collider

The Large Hadron Collider (LHC) based at CERN, in Geneva, is the largest particle accelerator, where proton-proton and heavy-ion collisions occur. At CERN, ambitious high-energy physics experiments that carry out the detection of particles based on particle-matter interaction processes are carefully planned, so that research about the matter that makes up our universe and new physics can keep on developing.

The LHC machine is a circular superconducting hadron accelerator and collider with a circumference of 26.7 km for the main ring, designed in such a way that it allows particle physicists to conduct studies at a very high energy scale of TeV.

In order to have particle-particle collisions, there are two counter-rotating beams that circulate around the ring within the same structure, and by doing so they cross the four interaction points where the four biggest experiments, ATLAS (Point 1), ALICE (Point 2), LHCb (Point 8), and CMS (Point 5) are installed.



(a) CERN accelerator complex.

Figure from Ref. [7].

(b) LHC beams schematic layout.

Figure from Ref. [5].

Figure 1: The CERN accelerator complex is shown on the left side. The LHC schematic layout of the clockwise and anticlockwise beams is shown on the right side.

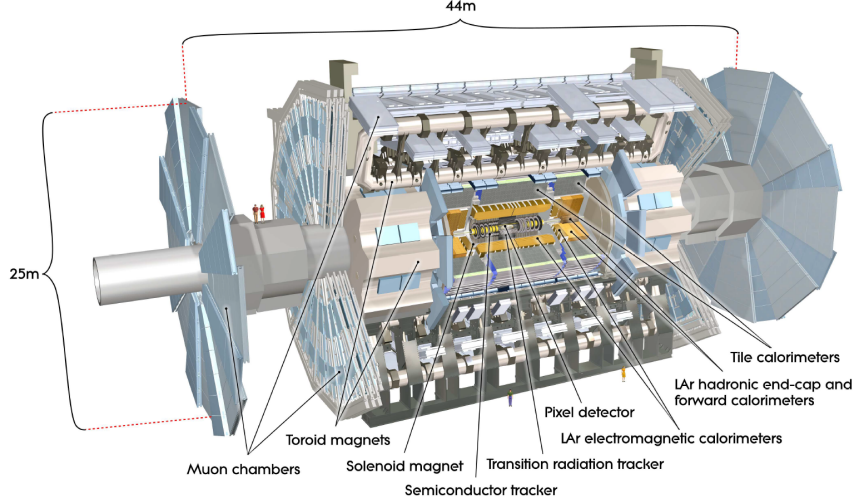


Figure 2: An overview of the ATLAS detector subsystems. Taken from Ref. [4].

1.2 The ATLAS experiment

The ATLAS (A Toroidal LHC ApparatuS) experiment is a multipurpose particle detector installed in the experimental cavern Point 1 of LHC at CERN. Similar to CMS (Compact Muon Solderoid) experiment, its purpose is to search and investigate particle events and prosperously new physics mainly from proton-proton collisions.

An overview of the different detector subsystems can be found in Fig. 2. The first subsystem that any particles traveling through the detector will encounter is the Inner Detector (ID). Since a subpart of the ID will be the main focus of this report, it will be explained in more detail in section 1.2.1.

Then there is the solenoid magnet. This subsystem has an influence throughout the detector, as the magnetic field generated by this magnet will affect the path of charged particles on their entire path. It is used for two things in particular. The direction the particles bend gives information on whether the particles are positively or negatively charged. If a particle does not bend at all, then the particle is neutrally charged. Secondly, the amount of bending the particles undergo gives the velocity of the particle. This information is used to determine the mass of the particle, and combined with the charge, it determines the type of particle that passed through the detector.

Next, the particles will encounter the two calorimeters. There are two, since different considerations have to be made for electromagnetic particles and hadrons. Hence, these

subsystems are called the LAr Electromagnetic Calorimeter (ECAL) and LAr Hadronic Calorimeter (HCAL) respectively. The prefix "LAr" here signifies that these calorimeters work with liquid argon. The purpose of these subsystems is to measure the energies of the types of particles they were designed for.

Lastly, there are the multiple layers of the muon spectrometer, where the momentum of muons is finally reached. These specialized layers are required, since the muon is a Minimally Ionizing Particle in the earlier detector layers and is thus not stopped by those layers.

All these layers attempt to give ATLAS researchers a complete overview of the interactions that happen in their detector.

1.2.1 The Inner Detector (ID)

In the Inner Detector, the primary source of radiation are charged hadron secondaries produced by inelastic proton-proton interactions at small radii. High-precision measurements are achieved by combining the Pixel Detector and Silicon Strip Tracker (SCT) with the straw tubes of the Transition Radiation Tracker (TRT). A cut-way view of the ATLAS ID can be seen in Fig. 3.

These precision tracking detectors are arranged in the barrel region on concentric cylinders around the beam axis, and on discs perpendicular to the beam axis in the endcap regions.

Positioned closest to the interaction point, the Pixel Detector provides fine spatial resolution, which is important for vertex reconstruction. It also significantly improves track reconstruction efficiency and momentum resolution, especially when it comes to low transverse momentum particles, and is designed to withstand the intense radiation environment. The Pixel Detector layers are segmented in $R - \phi$ and z , where each track crosses typically three pixel layers. There are approximately 80.4 million readout channels.

The Silicon Strip Detector features eight strip layers (corresponding to four space points) crossed by each track. In the barrel region, it uses small-angle (40 mrad) stereo strips to measure both coordinates, with one set of strips aligned parallel to the beam axis to measure $R - \phi$. Each module is composed of two daisy-chained sensors, each 6.4 cm long, with a strip pitch of 80 μm . In the endcap region, one set of strips runs radially, and another set is angled at 40 mrad. The SCT has a total of approximately 6.3 million readout channels.

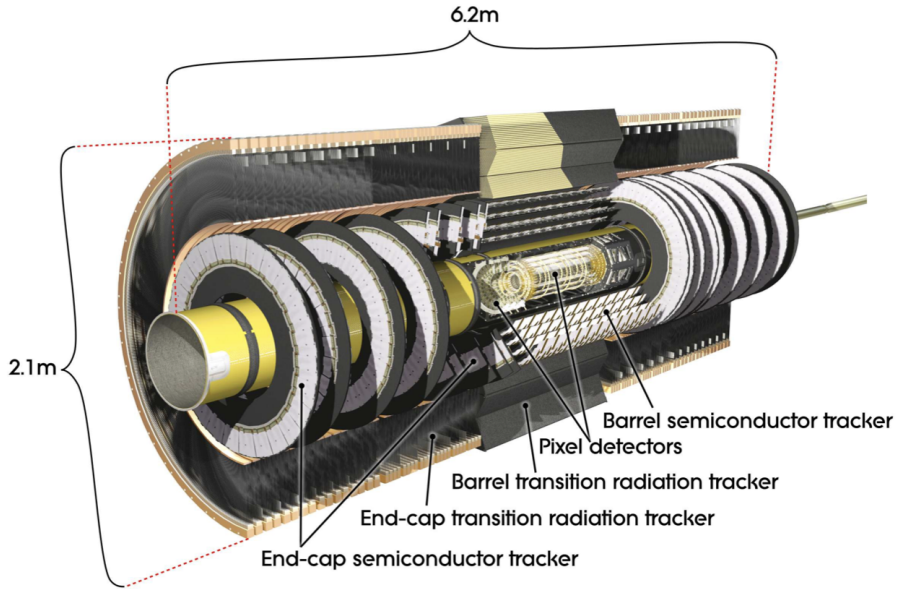


Figure 3: Cut-way view of the ATLAS Inner Detector. Taken from Ref. [1].

2 Silicon Strip Sensors

The Silicon Strip Detector is positioned in the second innermost layer of the ATLAS detector. Made from silicon which is a semiconductor, these detectors exploit the material's properties to detect charged particles by generating electron-hole pairs as the particles pass through.

A general description of semiconductor properties and their principle of operation is provided in the following paragraph.

2.1 Semiconductors

In solids (crystals), electron energy levels form bands rather than belonging to individual atoms. The structure of these bands plays a crucial role in determining the properties of solid-state detectors.

In a crystal there are some energy bands that are still bound states of the individual atoms, but then there are some bands that belong to the full crystal. The gap between the valence band and the conduction band is called the band gap.

If there are charges in the conduction band, then the crystal is a conductor.

If the conduction band is empty, and there is a large distance between it and the valence band, then the crystal is an insulator, because there are no movable charges.

And if the conduction band is empty but the band gap is small in energy, then there can always be thermal excitation and a few charges can always get into the conduction band, then the crystal is a semiconductor. So a semiconductor is a material between a conductor and an insulator.

The subject of our experimental study is a silicon crystal, a typical semiconductor that has four valence electrons and a band gap of 1.107 eV.

In semiconductors, the movement of charge carriers, which are the electrons (in the conduction band) and holes (missing electrons in the valence band), under an electric field allows for the flow of the electric current. The conductivity of semiconductors depends strongly on the temperature and doping.

As temperature increases, more electrons gain enough energy to cross the band gap into the conduction band, increasing the number of charge carriers and thus the conductivity. Doping introduces additional electrons (n-type) or holes (p-type) into the material, greatly enhancing conductivity even at lower temperatures.

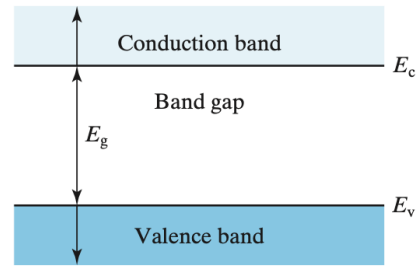


Figure 4: Energy band diagram of a semiconductor. Taken from Ref. [6].

2.2 The p-n junction

Conduction in the n-type semiconductor is carried out by electrons, while in the p-type semiconductor it is carried out by holes.

A p-n junction is created when both of these semiconductor materials are joined together. Then, electrons will diffuse from the n-side (leaving behind positively charged donor atoms) to the p-side (leaving negatively charged acceptor atoms), while holes from the p-side to the n-side. This diffusion creates a net current, leading to a buildup of negative charge on the p-side and positive charge on the n-side. As a result, a strong electric field develops across the junction, pointing from the n-side to the p-side.

A dynamic equilibrium quickly forms between diffusion and drift, characterized by a

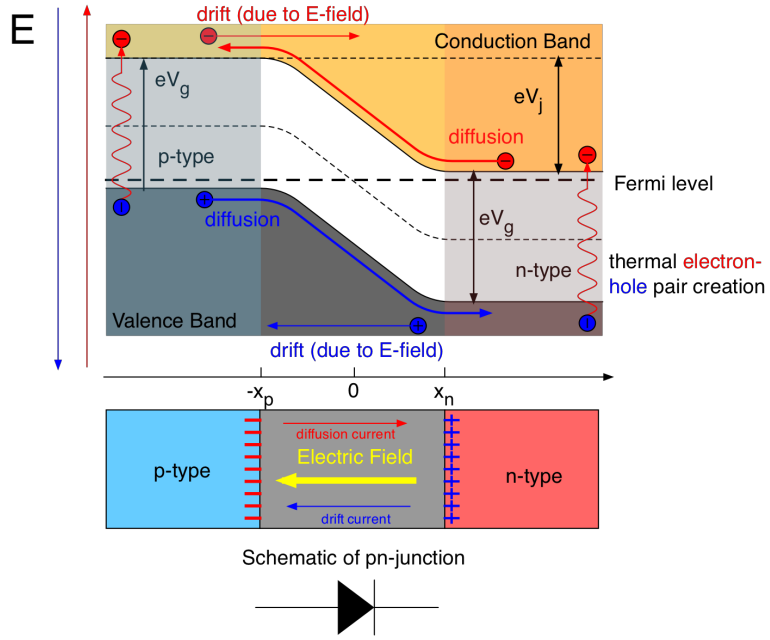


Figure 5: Charge carriers dynamics and the p-n junction. Taken from Ref. [9].

material-dependent potential called the diffusion voltage U_D , which is of the order of a few mV.

When an external reverse bias is applied, with the p-side connected to a negative voltage and the n-side to a positive voltage, the electric field across the junction strengthens. This drives free carriers away from the junction, enlarging the charge-free as the barrier layer or depletion zone. The thickness $d(U)$ increases with the applied bias voltage, influencing the junction's ability to detect or respond to external particles. This is described by the formula below:

$$d(U) = \sqrt{\frac{2\epsilon(U_D + U)}{qN_{eff}}} \quad (1)$$

where U is the applied voltage (bias voltage), U_D is the diffusion voltage, ϵ is the dielectric constant of silicon, q is the elementary charge, and N_{eff} is the effective charge carrier density of the crystal described by the following formula: $N_{eff} = \frac{N_D N_A}{N_D + N_A}$.

When the depletion region extends throughout the entire crystal, the material is said to be fully depleted. The corresponding bias voltage at which this occurs is called the depletion voltage U_{dep} , and it acts as a threshold for the applied voltage.

If the applied voltage is below this threshold, then only a fraction of the semiconducting material is depleting. The thickness of the depletion zone d_c can then be approximated as in the following:

$$d_c(U) = D \sqrt{\frac{U}{U_{dep}}} \quad \text{for } U < U_{dep} \quad (2)$$

$$d_c(U) = D \quad \text{for } U \geq U_{dep} \quad (3)$$

The detection of the energy deposited by an ionizing particle is possible when the sensor is fully depleted. That is because the internal electric field is spread over the entire volume of the semiconductor, ensuring that all electron-hole pairs are separated and collected before they recombine again. So ideally, in a fully depleted semiconductor there would be no free charge carriers, and hence no current flow.

But in reality, because of thermal excitation, electron-hole pairs are produced continuously. They are prevented from recombining again by the applied bias voltage and are collected at the electrodes, leading to a small but non-negligible *leakage current*.

As the bias voltage increases, the electric potential across the depletion zone also increases, and this leads to an increase of the leakage current as well. Typically, between the bias voltage and the leakage current there is an initial rapid increase which is then followed by a more linear one. This is shown in Fig. 6.

The transition point between these two regimes corresponds to the depletion voltage. After this point, additional voltage does not significantly enlarge the depletion zone, but may increase linearly the leakage current up to a the breakdown voltage, beyond which the semiconductor can get damaged.

By measuring the leakage current as a function of the applied bias voltage, the depletion voltage can be estimated from the shape of the resulting curve.

3 Experimental Setup

The components of the EASy detector system are the control unit, the detector unit and the computer software used for data acquisition, where the system operation is done via the Alibava-gui, a graphical user interface.

To set up the system, the detector unit is first connected to the control unit using a ribbon cable which supplies the detector with the necessary power and facilitates both data transmission and command communication. The control unit which is already connected to the detector unit, is then connected to the computer via a USB cable.

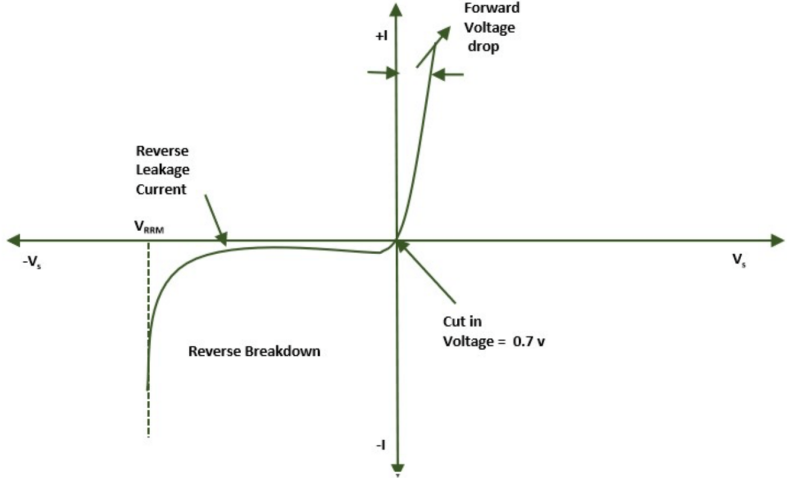


Figure 6: Current-Voltage characteristic of the p-n junction. Taken from Ref. [8].

3.1 Detector Unit

The detector unit consists of the silicon semiconductor sensor, similar to the one used in the ATLAS experiment, and the readout electronics chip BEETLE, which is connected to the strips of the silicon sensor via wirebonds.

The base of the silicon sensor consists of a thickness $D = 300 \mu\text{m}$, n-doped silicon layer, which is covered by a metal layer on the underside, and is connected to a low-ohmic resistor for power supply. The sensor is divided into 128 p-doped strips, insulated from each other, that are embedded in the n-doped base on the top.

The strip sensors are covered by a silicon oxide layer that prevents the leakage current from flowing directly into the readout electronics. On this layer, lies an aluminum electrode to which the p-doped implants are capacitively coupled to. In the images above, a schematic diagram of the silicon strip detector and a macroscopic view of a strip sensor can be seen.

Additional important elements of these

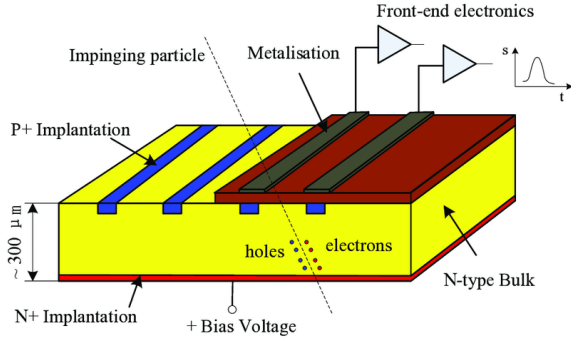


Figure 7: Schematic diagram of a silicon sensor.
Figure from Ref. [10].

types of sensors are the bias and the guard rings. The bias ring supplies the strips with voltage, while the guard rings keeps the charge flow under control, so that it doesn't go beyond the sensor into the electronics.

The BEETLE chip of the readout electronics converts the incoming charge signals into voltage signals, so it digitizes the signal and converts it into *ADC counts*. For the most efficient measurements, the silicon sensor must be fully depleted, and for the strip sensors, the depletion voltage is around $U_{dep} \approx (60 - 80)V$.

On top of the detector unit there is laser and a carbon plate, where the laser measures and examines the built-in strip sensors. It has a wavelength of 980nm, a diameter around 20 μm , a peak power of 0.6mW and a pulse length of 5ns. There are two micrometer screws, each adjusting the vertical and horizontal position of the laser with an accuracy of 10 μm .

3.2 Control Unit

The control unit controls the detector unit. Using the rotary knob "Diode Bias", the bias voltage of the sensor can be adjusted according to the task. The flowing leakage current is registered via an amperemeter of the control unit and can be read in 0.01 μA steps. Above the ribbon cable connector is a socket for an optical cable. The lemo connections are used for the trigger cable in the source measurement, with the radioactive source ^{90}Sr , where its decay chain follows the decay of ^{90}Y into ^{90}Zr through a β^- decay. Images of the full EASy system and the control unit is show in the following.



(a) Full units of EASy. Figure from Ref. [2].



(b) The control unit of the EASy system.
Figure from Ref. [2].

Figure 8: Image of the main components of the EASy system.

3.3 The Alibava-gui Software

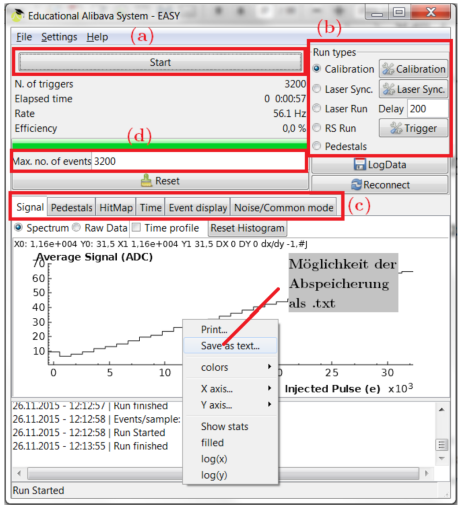


Figure 9: The main window of the Alibava graphical user interface .

The Alibava graphical user interface is used to control the Alibava system. It is written in C++ and manages the Control Unit of the EASY system. It enables device configuration, facilitates data acquisition through the USB, and saves the collected data for later analysis. During acquisition, it also offers live data monitoring. An image of the the main window when the Alibava runs is shown in Figure 9.

In the (a) area, the data recording can be started. In (b) one can determine the operating mode, and with (c) the display of the data can be selected. In (d) the size of the statistics can be determined.

4 Data Analysis

In this section, we will lay out the procedure, plots and results from the tasks we performed in the laboratory.

4.1 Influence of ${}^{90}\text{Y}$ and measurement of a current-voltage characteristic

The silicon strip sensor is examined in a later energy spectrum measurement using the radioactive source ${}^{90}\text{Sr}$ that decays by β^- emission into ${}^{90}\text{Y}$ as shown in the following decay chain:



The decay of ${}^{90}\text{Y}$ to ${}^{90}\text{Zr}$ affects the measurement because it emits much higher-energy β^- particles. Therefore, the measured energy spectrum, which is the distribution that describes the deposited energy, will have a broader, longer tail, as the high-energy electrons can penetrate much further and deposit much more energy.

To determine the depletion voltage, U_{dep} , of the silicon strip detector, we measured the current-voltage characteristic in 10V steps. This was to be confirmed if it agrees with the value that is stated by the manufacturer, $U_{dep} \approx (60 - 80)V$.

The plot in Fig. 10 shows the two main regions of the silicon detector in reverse-bias, the initial steep rise and the linear one, showing the typical behavior of semiconductors. This is in alignment with the fact that at low reverse bias, there is only partial depletion of the sensor, and as the bias voltage keeps increasing, the depletion region widens and the leakage current increases rapidly, non-linearly. The curve will change its behavior once it reaches the transition point, because then the detector is ideally fully depleted and the current will increase with the voltage but this time more slowly, in a linear manner. Therefore we estimated by looking at the point where the curve is flattening, a depletion voltage of $U_{dep} \approx 80V$.

A bias voltage of 20V higher than the estimated depletion voltage is applied, because in reality the depletion voltage itself is not enough to fully deplete the detector since the detector itself is not perfectly manufactured and there are parts that won't be able to get fully depleted at that threshold value. Applying a 20V higher bias voltage can make the full depletion of the detector. The reason we aim to have this is that, since the detector is sensitive to radiation, due to the ionization effect when charged particles pass through

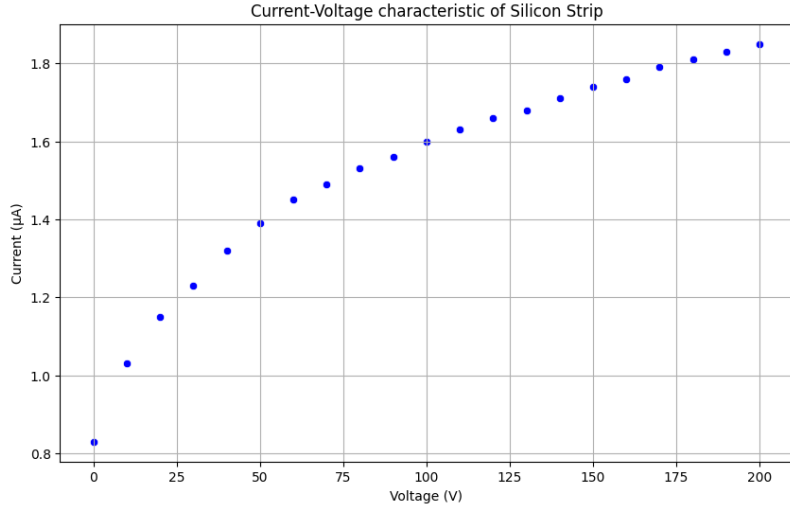


Figure 10: Current-Voltage characteristic curve for the silicon strip sensor. The transition from the non-linear to the linear region indicates that the sensor is fully depleted, with a depletion voltage of $U_{dep} \approx 80V$.

the material, if the depletion zone is wider, then there is more material for particles to pass through, which will cause a stronger effect and a stronger, larger signal. The detector is more efficient in collecting the charge, so this will lower the electronic noise, improving the signal-to-noise ratio as well. Being at a higher voltage than the depletion voltage is also useful to avoid measuring near the undepleted region where the leakage current fluctuations are present.

4.2 Pedestals and noise

After the depletion voltage was determined, in this next step we study the behavior of the detector. Since the sensor and readout electronics will always generate noise, it is very important to have this investigated, as it can interfere with the meaningful signal we are interested in.

To perform this analysis, some terminology and equations are necessary to introduce. A measured Analogue-to-Digital Converter (ADC) count, written as $\text{ADC}(i, k)$, where i is the strip number and k is a signal number, can be divided into three constituents

$$\text{ADC}(i, k) = P(i) + D(k) + \text{Signal}(i, k). \quad (4)$$

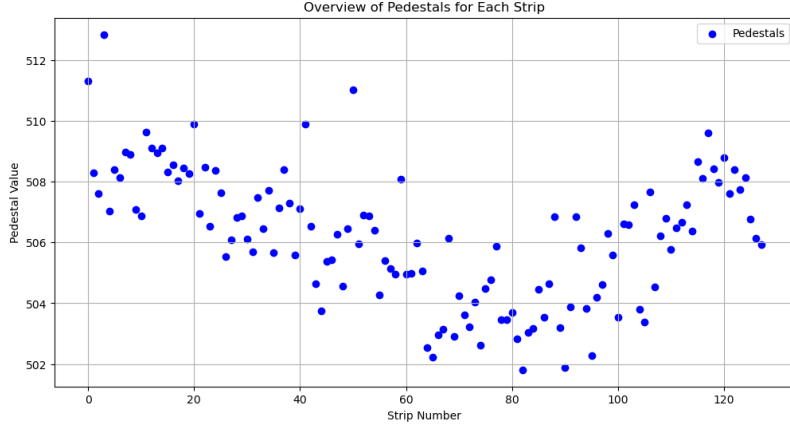


Figure 11: A scatterplot showing the Pedestals.

In this equation $P(i)$ is known as the pedestal. This is the mean value of the ADC counts for a certain strip i when there is no external signal. It is defined as

$$P(i) = \frac{1}{N} \sum_{k=1}^N \text{ADC}(i, k), \quad (5)$$

where N is the number of strips under consideration. As mentioned previously, in this experiment N is 128. A graphical representation of the pedestals can be found in Fig. 11. We can see that all values are slightly above 500. The next term in Eq. 4 is $D(k)$. This value is known as the Common Mode Shift, or the Common Mode. This value represents disturbances that affect all strips during any event. Since it depends only on the event, the value is thus equal for each strip in a given event. The expression for this measure is

$$D(k) = \frac{1}{N} \sum_{i=1}^N (\text{ADC}(i, k) - P(i)). \quad (6)$$

This value should be a Gaussian distributed around 0. As shown in Fig. 12, our data can be viewed as a Gaussian, although there seems to be a larger tail to the right. Lastly, we are interested in the noise of the strip. This is defined as the Root-Mean-Square (RMS) of the ADC counts, minus the pedestal and Common Mode Shift values. Mathematically, this can be expressed as

$$\text{Noise}(i) = \sqrt{\frac{1}{N-1} \sum_{k=1}^N (\text{ADC}(i, k) - P(i) - D(k))^2}. \quad (7)$$

We have plotted these values per strip in Fig. 13.

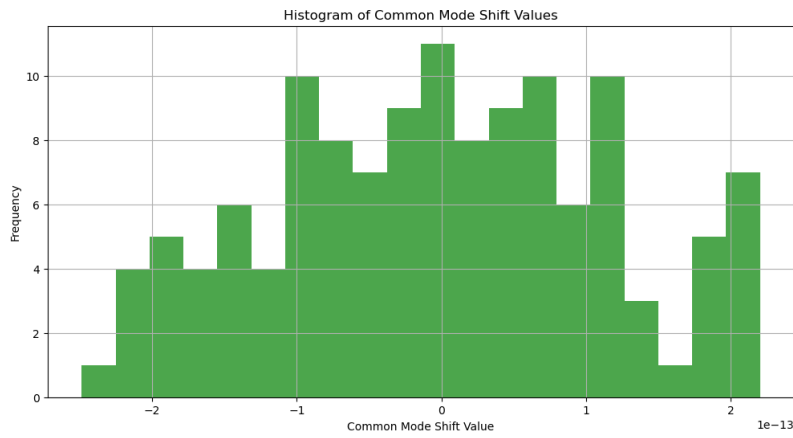


Figure 12: A histogram showing the distribution of the Common Mode (Shift). The data follows a Gaussian distribution with an increase in the far right tail.

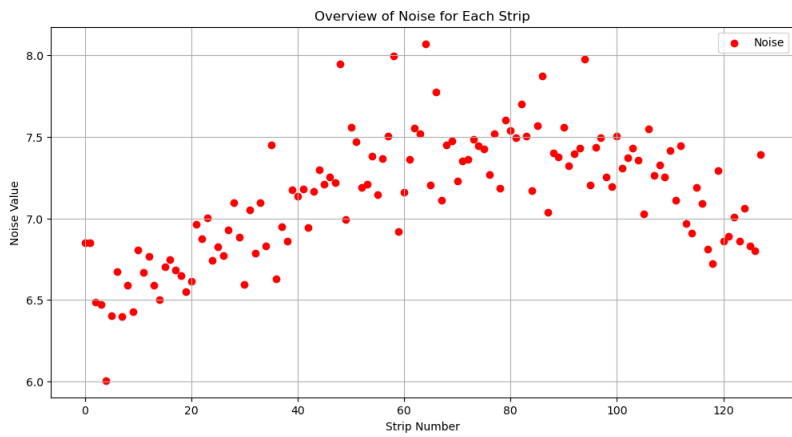


Figure 13: A scatterplot showing the noise for each strip.

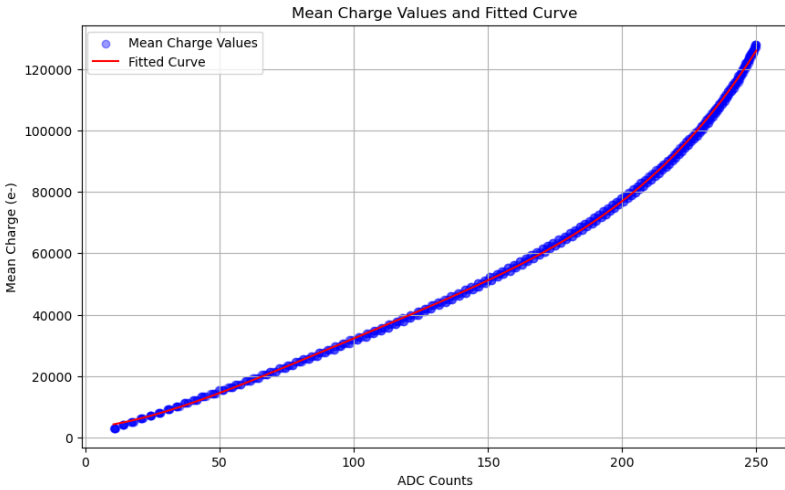


Figure 14: A plot showing the mean calibration data as well as the fit

4.3 Calibration measurements

The goal of this section is to show the calibration measurements performed that are also used in the later tasks. In particular, we obtain a fit that allows us to convert the ADC counts to electron-charge pairs, which is used in Section 4.7 to obtain the energy spectrum from the ADC spectrum.

To perform this analysis, we performed a Calibration Run in the software. During this Run, the control unit sends a defined electron pulse to the BEETLE, which then sends back the measured ADC counts. After the *Delay* scan, we determined an optimal delay value of 65ns, that was used then entered in the DAQ window for the following measurements.

We performed five runs where the bias voltage was set to 80V, 20V above the depletion voltage. During each of these runs we looked at different channels. We then calculated the mean charge values per ADC value, and created a fit based on these values. Both of these measures are plotted in Fig. 14. The coefficients obtained from these plots are used later in Sec. 4.7.

Additionally, it is of interest to see the effect of the bias voltage, therefore we also performed a run at a bias voltage of 0V, on channel 84 that we also used previously. We performed fits and plotted the charges in Fig. 15, where we can see that applying a bias voltage above the depletion voltage generally reduces the charge pairs associated with a specified number of ADC counts.

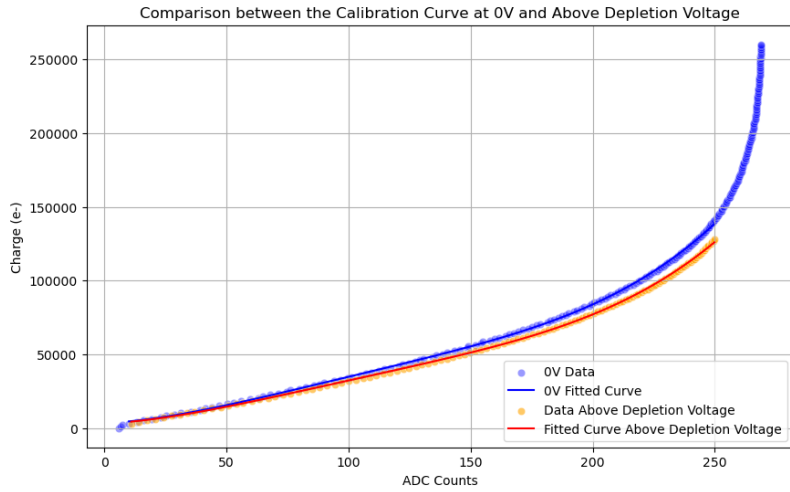


Figure 15: A plot showing the difference between applying a bias voltage of 80V and a bias voltage of 0V.

4.4 Measuring the strip sensors by using the laser

In this section we studied the structure of the built-in strip sensors and estimated an important parameter such as the pitch of the strips, by using the laser that is built into the system.

In order to do this, we first had to synchronize the laser with the system by selecting the operating mode *Laser Sync* in the graphical interface window, and started data acquisition. This is important because the strip sensors detect charge when a laser pulse creates electron-hole pairs in the silicon. Thus, the synchronization between the laser and the readout electronics ensures that the sensor signals are captured at the right time. As a result we got the measured ADC counts for all 128 strips of the silicon sensor.

We determined an optimal delay between the laser signal and the chip readout of 110ns.

After synchronizing the laser, we performed a *Laser Run* where the signal of each individual strip can be measured. Using the vertical micrometer screw for focusing and the horizontal one for positioning the laser over the strip, we adjusted the laser until we could see a peak, which corresponded to a signal detected by a strip.

We recorded 1000 events for 35 points by turning the horizontal micrometer screw at 10 μm intervals.

After getting the data, in order to plot the signal of relevant strips, we first had to identify them by looking at the Mean ADC Value with respect to the strip number for all 128

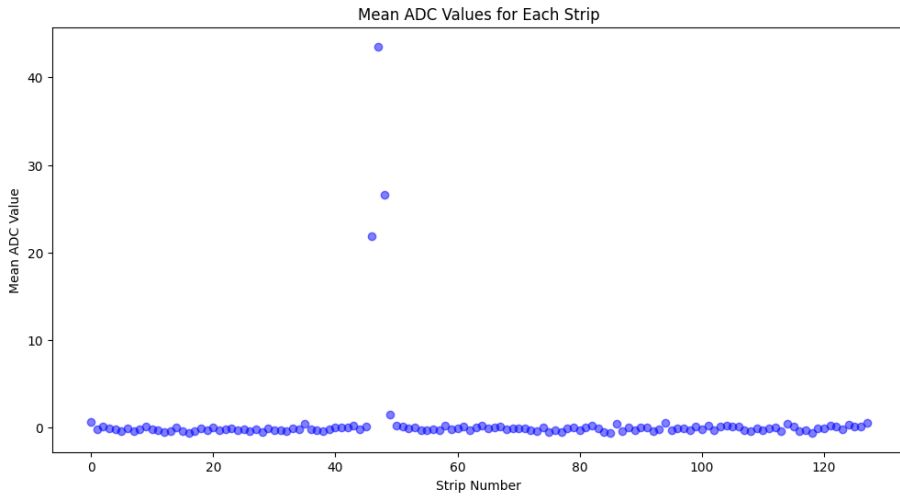


Figure 16: A scatter plot showing the Mean ADC Value for each individual strip. The plot is used for visual understanding and to help identify how many strips have had a peak signal during the Laser Run. From the analysis, the relevant strips are those numbered 47, 48 and 49.

strips as shown in Fig. 16. The purpose of this plot is to identify how many and what specific strips have had a peak signal, so that they can be used to determine the pitch of the strips in the next step.

The final plot showing the signal of all the three relevant, adjacent strips numbered 47, 48 and 49 is shown as a function of the laser position in Fig. 17.

The pattern that is shown on this plot is in alignment with the expected response of the silicon strip sensor and the effectiveness of the laser spatial adjustment during the scan. The peaks of each strip correspond to the position of the laser when it is directly above the strip. The certain laser positions where there is no signal detector by the strips, can be explained with the fact that the laser is being reflected by the metallisation layer in the middle of the strips, instead of penetrating the silicon, and that is why there are no electron-hole pairs generated and therefore no signal measured. As it is shown, the pattern is repeated for the three strips to the extent of what we see on the figure.

By marking the positions of the maximum signal for each of the strips, we determined the pitch of strips. That is because the pitch of strips is defined as the distance between the peaks of two adjacent strip sensor, and it is a valuable parameter to measure because it contains information regarding the spatial and position resolution of the detector, and

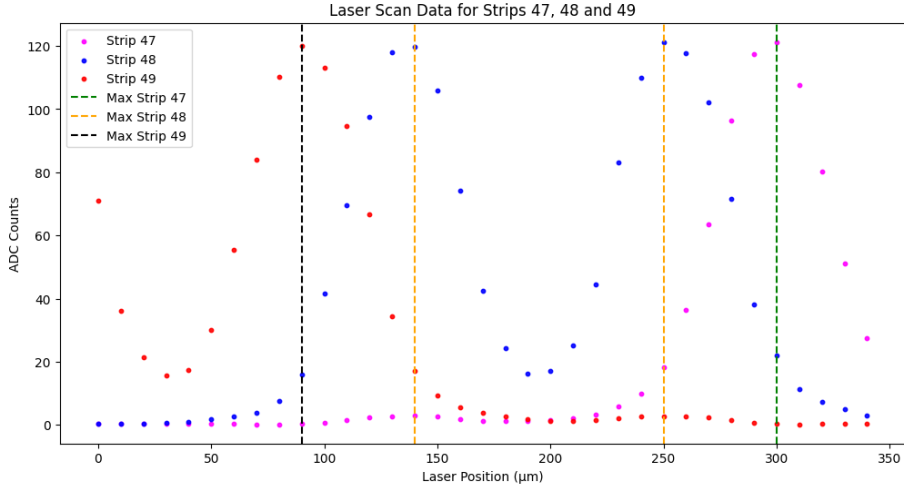


Figure 17: A scatter plot showing the signal of three adjacent strips 47, 48 and 49 as a function of laser position. The vertical dashed lines mark the maximum signal that is read from each strip.

it is useful for reconstructing the position of laser pulses or charge hits. We found the pitch of the strip sensors to be $(160 \pm 10)\mu\text{m}$.

4.5 Determination of the Charge Collection Efficiency: Using a laser

This section studies the Charge Collection Efficiency (CCE) which is measured first using a laser and then using a β^- source which is discussed in Section in 4.6.

Here we followed a similar procedure as in the preceding section, but in this case, the horizontal and vertical position of the laser were kept fixed, and we varied the applied bias voltage from 0V to 200V in 10V steps and recorded a dataset of 1000 events for every voltage.

In our analysis, the number of ADC Counts is summed over all the events and then divided by the maximum number found in the total sum in order to get the normalized efficiency shown in Fig. 18. The CCE is proportional to the thickness of the depletion zone until it reaches its maximum value which corresponds to the depletion voltage, which in our measurement is determined to be approximately $U_{dep} \approx 80\text{V}$. Ideally, after the depletion voltage, the CCE would continue to grow more slowly, almost remaining constant close to 1. As it can be seen from the plot, the CCE is indeed growing more

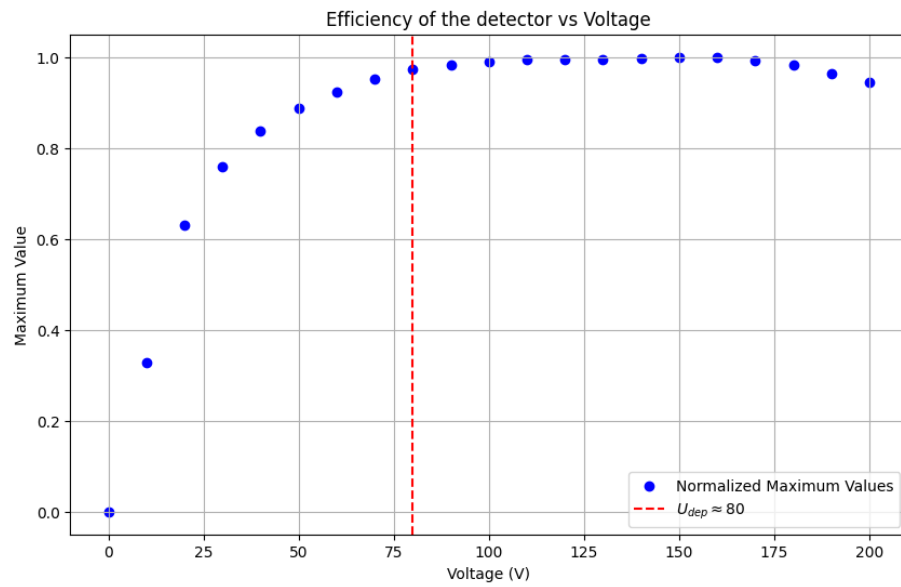


Figure 18: Charge Collection Efficiency of the detector where the counts are summed over all the events, divided by the maximum number of counts to normalize the efficiency. The CCE reaches its maximum value at $U = U_{dep}$, and then remains almost constant for higher voltages.

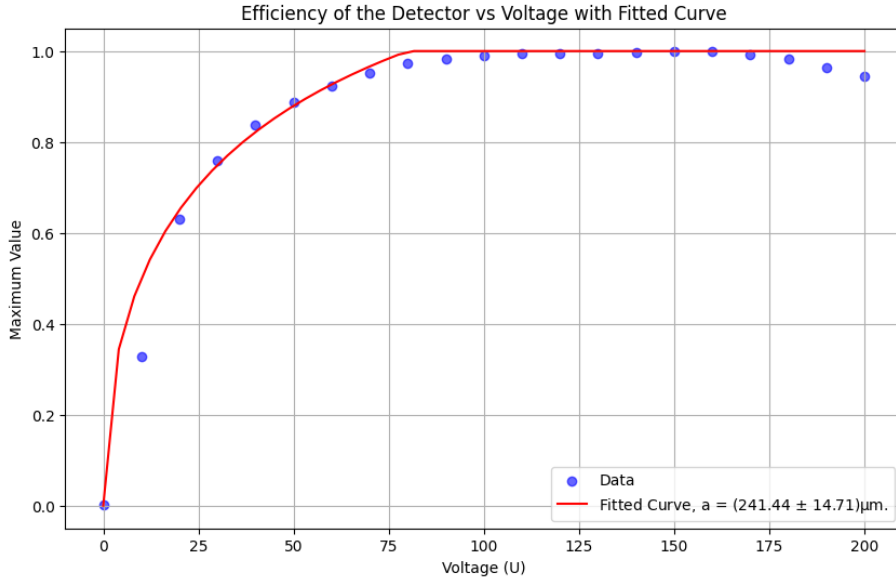


Figure 19: Charge Collection Efficiency of the detector curve with the corresponding fit from Equation 8, where the penetration depth is estimated to be $a = (500.00 \pm 240.24)\mu\text{m}$.

slowly at voltages that are higher than the depletion voltage, but also some small fluctuations are also seen when the voltage exceeds the value around $U \approx 160\text{V}$.

Using the relation given in equation 8 between the CCE, thickness of the depletion zone $d_c(U)$, the sensor thickness given by the manufacturer as $D = 300\mu\text{m}$, and the penetration depth of the laser a , we can determine the latter one via a curve fit.

$$CCE(U) = \frac{1 - \exp\left(\frac{-d_c(U)}{a}\right)}{1 - \exp\left(\frac{-D}{a}\right)} \quad (8)$$

where the depletion zone behavior is given from equations 2 and 3. The fit of the curve and the estimated parameter for the penetration depth $a = (500.00 \pm 240.24)\mu\text{m}$ is shown in Fig. 19. It is worth noticing that the CCE curve of our data starts to drop in the last three measurements, which is an unexpected behavior, as the curve should ideally be saturated and remain constant in the region where the voltage is higher than the depletion voltage. However, this could happen at voltages much higher than the depletion voltage and probably has to do with the increasing kinetic energy of the created electron-hole pairs.

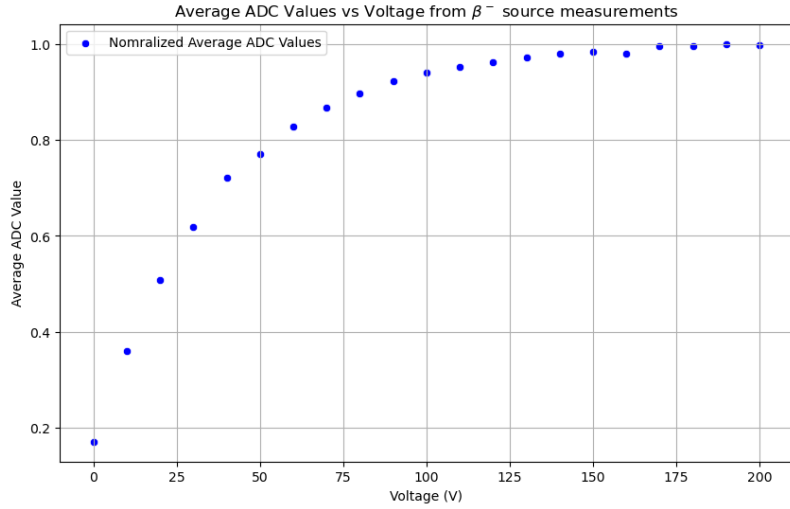


Figure 20: A plot showing the relation between the applied bias voltage and the normalized measured ADC counts from a β^- .

4.6 Determination of the Charge Collection Efficiency: Using a β^- source

For this section, a similar analysis from the laser was to be performed, but now using a real β^- source. However, due to a hardware malfunction, we were unable to collect this data ourselves, and we were supplied with the data by the supervisor.

Similarly to the previous section, we calculate the average ADC value for each voltage level and plot the result. This plot is shown in Fig. 20.

We then compare this measurement to the laser, by overlaying the two plots. The result of this is shown in Fig. 21.

There appear to be three major differences. Firstly, we notice that for the laser, the ADC counts start at 0 for an applied bias voltage of 0V. However, the same voltage for the β^- source already shows a signal of slightly below 0.2. This happens because there is still activity even when there is no voltage applied, as the source is still emitting β particles. Secondly, the slope of the laser scan data is higher, which means that the laser scan data reaches the maximum faster than the source data, even though it starts lower. Lastly, in the saturation region where both curves are expected to be almost constant, we see that the β^- source measurement shows this behavior, while the laser measurement drops a little as discussed in the previous section 4.5.

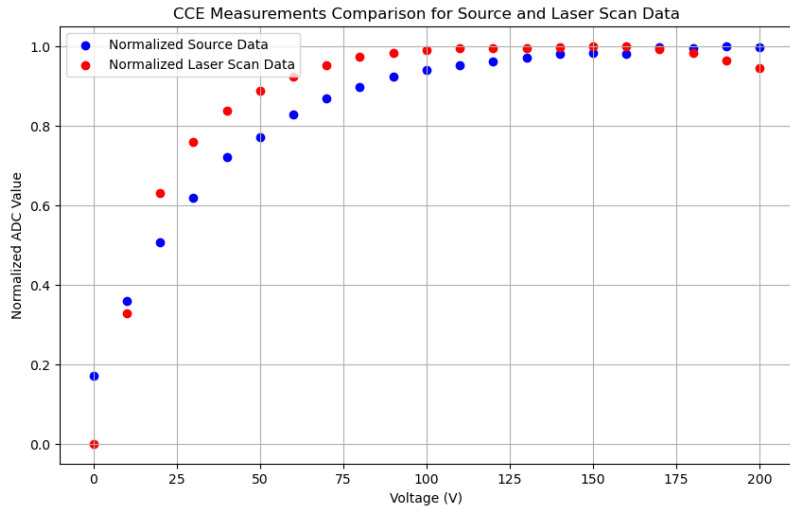


Figure 21: A plot showing the normalized ADC values for both the β^- source and the laser

4.7 Large source scan

Due to the issues mentioned in the previous subsection, we also could not perform this measurement ourselves, so the data used was provided by our supervisor. This data represents a continuous run of 1,000,000 events, and was preprocessed before being given to us, with a signal-to-noise cut. The preprocessing code also determines the pedestals, noise and common mode shift, as well as generating clusters. This is thus the data that we used for the following analysis.

In order to get an idea of the behaviour of the clusters, we created two plots. The first, shown in Fig. 22, shows the number of clusters that were measured for each event. We notice that while there are some events that formed no clusters, and some events that formed multiple clusters, the large majority of events formed one cluster.

The second, shown in Fig. 23, shows the number of channels that formed each cluster. We notice that there seems to be an exponential decrease in the number of channels that each cluster contains.

Then, in order to discover the distribution of hits on the detector, and thus find information on how the source was positioned in the detector, we created a histogram that shows the number of hits on each channel/stripe. The results of this can be found in Fig. 24. We notice a Gaussian-like distribution with a peak at around strip 75-80. From this

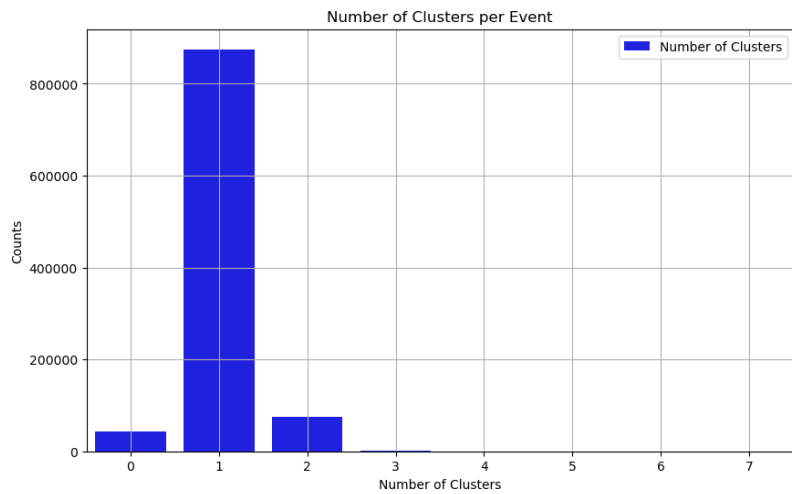


Figure 22: A histogram that shows the distribution of the amount of clusters per event.

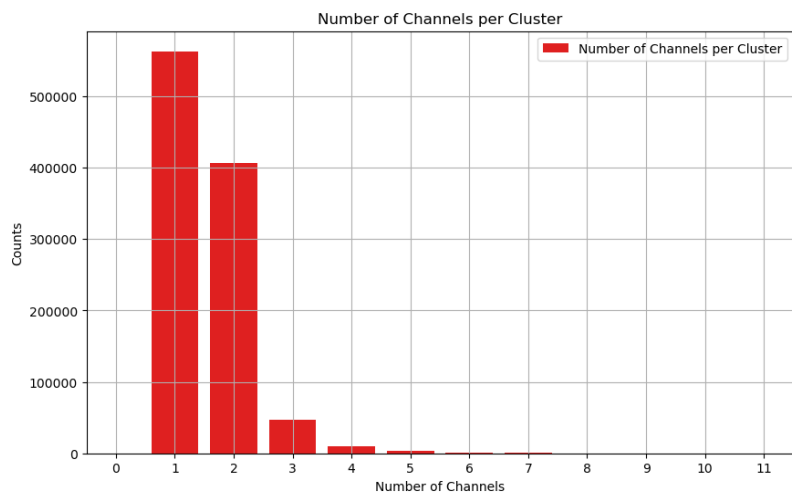


Figure 23: A histogram that shows the number of channels that formed a cluster.

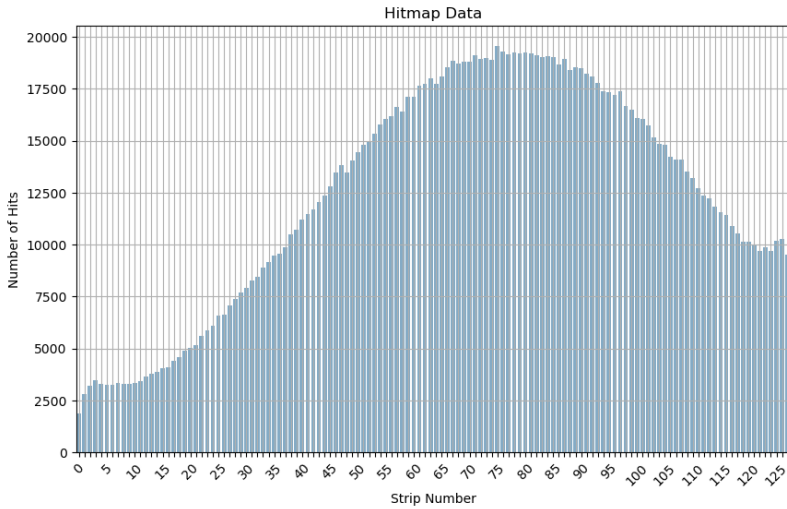


Figure 24: A histogram showing the distribution of where there were hits on the detector.

we deduce that the source was closest to this area of the detector.

The next step we took was to find the energy spectrum of the ^{90}Sr decay. This can give insights into the inner workings of the decay. We first did this as a function of the ADC counts. This histogram, along with the Most Probable Value (MPV) and mean can be found in Fig. 25. We see the expected distribution, with a sharp MPV peak around 79 ADC Counts, and a mean around 94.6 ADC Counts, which corresponds with the strong right tail.

However, it is more interesting to consider the values in actual units of energy. In this case, we chose to work in keV, as this is a good scale to work at. For this, we used the fit we made in Sec. 4.3 to transform the number of ADC counts to charge, which corresponds to electron-hole pairs. Then, by using the conversion factor that it takes 3.6 eV of energy to create an electron-hole pair in silicon, we are able to find the energy spectrum in keV, which is shown in Fig. 26. We see a similar distribution, but with a slightly heavier right tail. We find a mean of 106.6 keV, with a MPV of 93.9 keV.

This makes sense, since this is a thin tracking detector. The particle is in the great majority of cases not fully absorbed, which is why the observed mean energy of 106.6 keV is so much lower than both the average emission energy of 196 keV, as well as the maximum emission energy of 545.9 keV [3].

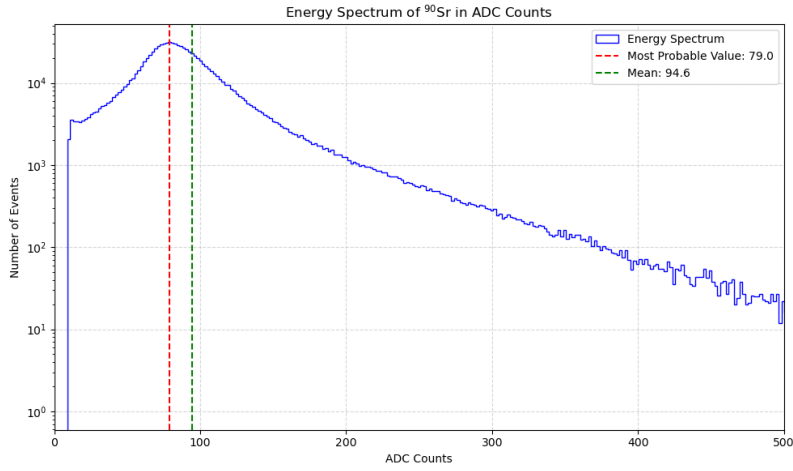


Figure 25: A histogram showing the distribution of the ADC counts of the β^- source, along with the MPV and mean.

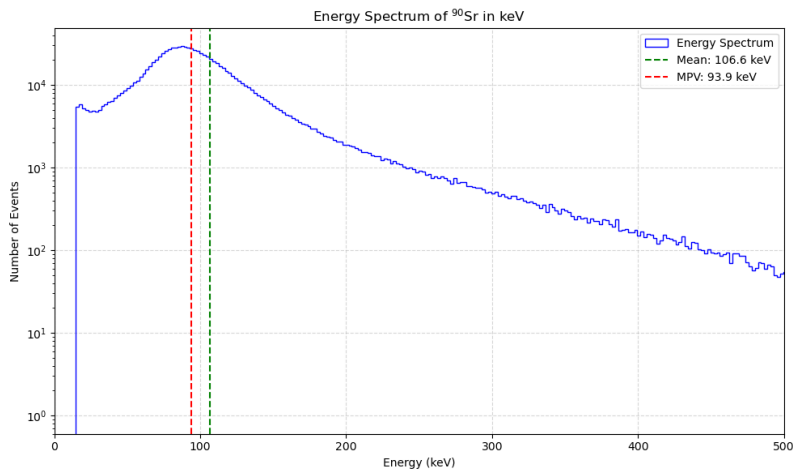


Figure 26: A histogram showing the distribution of the keV energy of the β^- source, along with the MPV and mean.

5 Conclusions

In this laboratory experiment we studied the silicon strip sensors and their properties using a laser and a ${}^{90}\text{Sr}$ radioactive source.

From the characteristic current-voltage of the silicon strip we confirmed the typical behavior of the silicon semiconductor and estimated a depletion voltage of $U_{dep} \approx 80\text{V}$, which is within the range given by the manufacturer.

In order to minimize background events, we investigated the behaviour of the Pedestals, the Common Mode Shift, and the Noise. We saw that these distributions behave as expected, so we expect no problems to arise from there.

We then performed a calibration measurement, which we use to relate the number of ADC counts to the charge. We ran this over five channels and found a reasonable fit. We also found that the influence of the bias voltage generally reduces the charge pairs associated with a number of ADC counts.

In the following measurements we investigated the structure of the 128 strip sensors using the laser, in order to estimate the pitch of the strips, which is an important characteristic parameter of the sensors. We found the pitch of the strip sensor to be $(160 \pm 10)\mu\text{m}$.

Next, we measured the Charge Collection Efficiency using the laser first. The CCE curve showed the expected behavior of increasing rapidly until reaching the depletion voltage, and then remaining almost constant in voltages higher than the depletion voltage. It was seen that the last three measurements had lower values, causing a noticeable drop in the saturation region.

Repeating this procedure for the β^- source, which we did not do ourselves due to a hardware malfunction, we investigated the difference between the effect of a β^- source compared to a laser, where we noticed differences in the starting position, slope, and saturation region.

Finally, we performed a large source scan, where we investigated the behaviour of clusters, as well as on what detector the most hits were found. Lastly, we performed an analysis on the energy spectrum, where we found that the mean energy deposition in the strip was 106.6 keV, while the MPV was 93.9 keV.

A combination of all these factors forms a characterization of of silicon strip sensors.

References

- [1] G. Aad et al. “The ATLAS Experiment at the CERN Large Hadron Collider”. In: *JINST* 3 (2008), S08003. doi: [10.1088/1748-0221/3/08/S08003](https://doi.org/10.1088/1748-0221/3/08/S08003).
- [2] Alibava Systems. *Easy System – Compact readout system for microstrip sensors*. Accessed: 2025-05-01. n.d. URL: <https://alibavasystems.com/product/easy/>.
- [3] Laboratoire National Henri Becquerel. *Table de Radionucléides $^{90}_{38}SR_{52}$* . Accessed: 2025-05-09. 2005. URL: www.lnhb.fr/nuclides/Sr-90_tables.pdf.
- [4] ATLAS Collaboration. “The ATLAS experiment at the CERN Large Hadron Collider: a description of the detector configuration for Run 3”. In: *JINST* 19.05 (2024). 233 pages in total, author list starting page 214, 116 figures, 15 tables, published in JINST. All figures including auxiliary figures are available at <http://atlas.web.cern.ch/Atlas/GROUPS/PHYSICS/PAPERS/GENR-2019-02/>, P05063. doi: [10.1088/1748-0221/19/05/P05063](https://doi.org/10.1088/1748-0221/19/05/P05063). arXiv: [2305.16623](https://arxiv.org/abs/2305.16623). URL: <https://cds.cern.ch/record/2859916>.
- [5] Lyndon Evans and Philip Bryant. “LHC Machine”. In: *Journal of Instrumentation* 3.08 (Aug. 2008), S08001. doi: [10.1088/1748-0221/3/08/S08001](https://doi.org/10.1088/1748-0221/3/08/S08001). URL: <https://dx.doi.org/10.1088/1748-0221/3/08/S08001>.
- [6] Chenming Hu. *Electrons and Holes in Semiconductors*. https://www.chu.berkeley.edu/wp-content/uploads/2020/01/Chenming-Hu_ch1-3.pdf. Accessed: April 29, 2025. 2020.
- [7] Esma Mobs. “The CERN accelerator complex in 2019. Complexe des accélérateurs du CERN en 2019”. In: (2019). General Photo. URL: <https://cds.cern.ch/record/2684277>.
- [8] TutorialsPoint. *Power Diodes - Power Electronics*. https://www.tutorialspoint.com/power_electronics/power_electronics_power_diodes.htm. Accessed: 2025-04-29. n.d.
- [9] W. Boeglin. *P-N Junction*. https://wanda.fiu.edu/boeglinw/courses/Modern_lab_manual3/pn_junction.html. Accessed: April 29, 2025. n.d.
- [10] Xiaomin Wei. “Study and improvement of radiation hard monolithic active pixel sensors of charged particle tracking”. In: (Dec. 2012).